






# Rapidly Spinning Compact Stars with Deconfinement Phase Transition

Tuna Demircik<sup>1,2</sup> , Christian Ecker<sup>3</sup> , and Matti Järvinen<sup>2,4</sup> 

<sup>1</sup> Department of Physics, Ben-Gurion University of the Negev, Beer-Sheva 84105, Israel; [ecker@itp.uni-frankfurt.de](mailto:ecker@itp.uni-frankfurt.de)

<sup>2</sup> Asia Pacific Center for Theoretical Physics, Pohang, 37673, Republic of Korea

<sup>3</sup> Institut für Theoretische Physik, Goethe Universität, Max-von-Laue-Str. 1, D-60438 Frankfurt am Main, Germany

<sup>4</sup> The Raymond and Beverly Sackler School of Physics and Astronomy, Tel Aviv University, Ramat Aviv 69978, Tel Aviv, Israel

Received 2020 October 8; revised 2020 December 1; accepted 2021 January 4; published 2021 January 29

## Abstract

We study rapidly spinning compact stars with equations of state featuring a first-order phase transition between strongly coupled nuclear matter and deconfined quark matter by employing the gauge/gravity duality. We consider a family of models that allow purely hadronic uniformly rotating stars with masses up to approximately  $2.9 M_{\odot}$ , and are therefore compatible with the interpretation that the secondary component ( $2.59^{+0.08}_{-0.09} M_{\odot}$ ) in GW190814 is a neutron star. These stars have central densities that are several times the nuclear saturation density, so that strong coupling and non-perturbative effects become crucial. We construct models where the maximal mass of static (rotating) stars  $M_{\text{TOV}}$  ( $M_{\text{max}}$ ) is either determined by the secular instability or a phase-transition induced collapse. We find the largest values for  $M_{\text{max}}/M_{\text{TOV}}$  in cases where the phase transition determines  $M_{\text{max}}$ , which shifts our fit result to  $M_{\text{max}}/M_{\text{TOV}} = 1.227^{+0.031}_{-0.016}$ , a value slightly above the Breu–Rezzolla bound  $1.203^{+0.022}_{-0.022}$  inferred from models without phase transition.

*Unified Astronomy Thesaurus concepts:* Neutron stars (1108); Neutron star cores (1107); Nuclear astrophysics (1129)

## 1. Introduction

The Laser Interferometer Gravitational-Wave Observatory (LIGO)/Virgo Collaboration recently announced the gravitational wave event GW190814 (Abbott et al. 2020). This event was identified as the merger of a  $23.2^{+1.1}_{-1.0} M_{\odot}$  black hole (BH) and a  $2.59^{+0.08}_{-0.09} M_{\odot}$  object making it the detection of a binary merger with the most unequal mass ratio  $0.112^{+0.008}_{-0.009}$  so far. While the primary component is conclusively a BH, the nature of the lighter companion remains unclear. It falls into the so-called mass-gap region and is either the lightest BH or the heaviest neutron star (NS) ever observed in a binary system. The secondary component is significantly heavier than the most massive known pulsars, including PSR J1614-2230 ( $1.908^{+0.016}_{-0.016} M_{\odot}$ ; Arzoumanian et al. 2018), PSR J0348+0432 ( $2.01^{+0.04}_{-0.04} M_{\odot}$ ; Antoniadis et al. 2013), and MSP J0740+6620 ( $2.14^{+0.1}_{-0.09} M_{\odot}$ ; Cromartie et al. 2019). The mass of the secondary component is also well above the upper bound on the maximum mass of non-rotating NSs  $\approx 2.3 M_{\odot}$  determined from the electromagnetic counterpart of GW170817 (Rezzolla et al. 2018; Shibata et al. 2019).

The possibility that the lighter companion could be a rapidly rotating NS, or a small BH of that origin, was pointed out in Most et al. (2020) and used to determine a lower bound on the maximum mass  $M_{\text{TOV}} < 2.08^{+0.04}_{-0.04} M_{\odot}$  of non-rotating stars.

There exist already a number of studies addressing the nature of the smaller companion of GW190814 and its compatibility with a rapidly rotating NS (Dexheimer et al. 2020; Essick & Landry 2020; Fattoyev et al. 2020; Godzieba et al. 2020; Roupas 2021; Safarzadeh & Loeb 2020; Tews et al. 2020; Zhang & Li 2020), a non-rotating star (Fattoyev et al. 2020; Tan et al. 2020), or a primordial BH (Vattis et al. 2020). The latter two options, however, were found to be rather unlikely.

We argue that there is an important strong coupling aspect to this question. Namely, the maximal mass of rotating ( $M_{\text{max}}$ ) and static ( $M_{\text{TOV}}$ ) NSs is sensitive to the equation of state (EoS)

at high density where effective nuclear theory models become unreliable and the gauge/gravity duality (or holography for short) may be better suited. The main purpose of this Letter is to investigate compatibility of state-of-the-art holographic models for cold and dense cold and dense matter in quantum chromodynamics (QCD) matter with the hypothesis that the smaller companion in GW190814 was a rapidly rotating NS. We also compare our results to the universal mass ratio  $M_{\text{max}}/M_{\text{TOV}} = 1.203^{+0.022}_{-0.022}$  proposed in Breu & Rezzolla (2016).

An interesting prediction of the holographic model that we are using (V-QCD model; Järvinen & Kiritsis 2012) is the presence of a strong first-order nuclear to quark matter phase transition. Quark and hybrid stars with  $M > 2M_{\odot}$  and a first-order transition have been constructed in Weissenborn et al. (2011) assuming absolutely stable strange quark matter, and generic conditions for the stability of such stars were derived in Alford et al. (2013). Signatures of phase transitions in binary NS mergers were studied in Bauswein et al. (2019), Most et al. (2019), Ecker et al. (2020), and Weih et al. (2020). In this Letter we, in particular, analyze how the phase transition affects the results derived from the data for GW190814. We remark that the V-QCD model is one of the very few models that is able to describe both the nuclear and quark matter phases, and therefore the phase transition, in a single framework.

The rest of this Letter is structured as follows. In Section 2 we introduce the holographic EoSs that we are studying. In Section 3 we discuss the model for rotating stars that we are using and their stability. In Section 4 we present results for the NS properties and mass–radius curves. Finally, in Section 5 we summarize and conclude. Unless stated otherwise, we use units where  $c = G = 1$ .

## 2. EoS

We follow an approach (Ecker et al. 2020; Jokela et al. 2020) where the strongly coupled bulk of the NS is modeled by

employing the gauge/gravity duality, whereas a traditional field theory approach is used for the crust.

The holographic V-QCD model is a fusion of improved holographic QCD (Gursoy & Kiritsis 2008) for the glue dynamics and an approach to include quarks based on brane actions (Bigazzi et al. 2005; Casero et al. 2007). This approach is effective: the model contains a large number of parameters that must be determined by comparing to QCD, i.e., requiring agreement with general properties such as confinement and discrete spectrum, and in the end by comparing to lattice data. For the latter, we use the results from Jokela et al. (2019), where the predictions of the model were compared both to lattice data for the EoS of pure Yang–Mills (Panero 2009) and to lattice data for the EoS and the baryon number susceptibility of full QCD with  $2 + 1$  dynamical quarks in the quark-gluon plasma phase (Borsanyi et al. 2012, 2014). In a similar spirit, simple holographic bottom-up models have been carefully fitted to lattice data, and thereafter used to gain insights about the critical point in the QCD phase diagram (DeWolfe et al. 2011a, 2011b).

We study three different versions of V-QCD, referred to as soft, intermediate, and stiff, obtained through different fits to lattice QCD data in Jokela et al. (2019).<sup>5</sup> As an important constituent for the current study, nuclear matter was included in the model by using a simple approximation scheme in Ishii et al. (2019), which models isospin symmetric nuclear matter through a homogeneous dual configuration. This model has been employed previously in NS merger simulations (Ecker et al. 2020), and to study the properties of QCD and static NSs based solely on predictions for the quark matter phase (Chesler et al. 2019; Jokela et al. 2019; Hoyos et al. 2020) and including holographic nuclear matter (Jokela et al. 2020).

To model the crust we use the Akmal–Pandharipande–Ravenhall (APR; Akmal et al. 1998) EoS up to number densities  $n < 1.6 n_s$ , where  $n_s = 0.16 \text{ fm}^{-3}$  is the nuclear saturation density. The point  $n_{\text{tr}} = 1.6 n_s$ , where we match the holographic model with the low-density nuclear matter model, is our estimate for the density where the holographic approach becomes more reliable than the traditional (effective field theory) approach. NSs with high masses, which are the focus of this letter, are mostly sensitive to the high-density regime described by holography in our approach. This has been shown in Jokela et al. (2020) by analyzing a larger set of “hybrid” EoSs of this kind, with various other nuclear models for the crust (in addition to APR) and spanning a wide range of values of  $n_{\text{tr}}$ . We will also verify this here by carrying out a scan of basic observables over such a set of EoSs. All EoSs in this work assume beta equilibrium (which in the isospin symmetric high-density nuclear matter regime implies zero electron density) and zero temperature.

In Figure 1 we show the three EoSs together with theoretical uncertainties in nuclear theory (Tews et al. 2013; blue band) and perturbative QCD (Kurkela et al. 2010; orange band) at low and high density, respectively, and bounds from causality and current astrophysical observations in between. Notice that perturbative QCD not only constrains the EoS at asymptotically high densities, but also narrows the uncertainty band at intermediate densities (Kurkela et al. 2014). We show two different bands at intermediate densities. The light blue band is

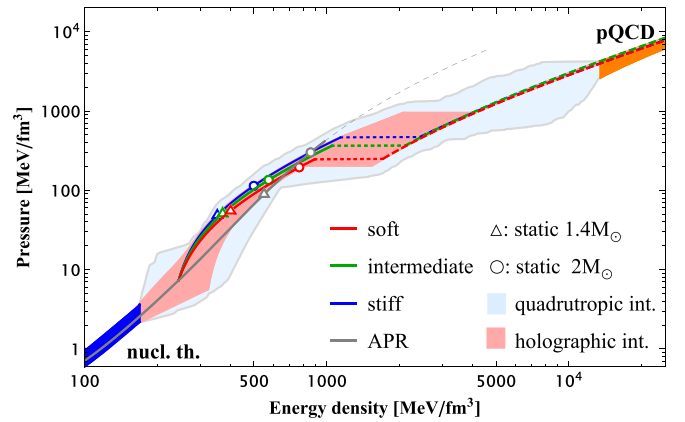


**Figure 1.** EoSs. Red, green, and blue curves are the V-QCD EoSs where first-order phase transitions are indicated by dotted lines and the quark phases by dashed lines. Gray curve is the APR EoS whose superluminal part is the dashed part of the curve. Centers of static  $1.4 M_{\odot}$  and  $2 M_{\odot}$  stars are marked by triangles and circles, respectively. Blue and orange bands indicate uncertainty in nuclear theory and perturbative QCD, respectively. The light red (light blue) band is spanned by holographic (general quadrupole) interpolations between the low- and high-density limits.

spanned by quadrupole interpolations (following Annala et al. 2018) between the low- and high-density results, which also satisfy the astrophysical bounds: the maximal mass of static NSs is at least  $2 M_{\odot}$  and the tidal deformability  $\Lambda_{1.4}$  (at NS mass  $M = 1.4 M_{\odot}$ ) is less than the bound 580 obtained from the analysis of GW170817 by LIGO/Virgo (low-spin prior at 90% confidence level; Abbott et al. 2018). The light red band is spanned by the aforementioned larger ensemble of V-QCD EoSs, which satisfy the same bounds (Jokela et al. 2020).

Red, green, and blue curves are the V-QCD EoSs, which are matched at  $\approx 244 \text{ MeV fm}^{-3}$  to the APR curve shown in gray. Solid lines at low and intermediate densities correspond to the confined nuclear matter phase, dashed lines are in the deconfined quark matter phase, and dotted horizontal lines are mixed phases between the two. The thin dashed part of the gray curve is where the APR model has speed of sound larger than the speed of light, and therefore is clearly outside its range of applicability. We remark that potential spurious numerical effects caused by the discontinuity of the speed of sound (see, e.g., O’Boyle et al. 2020) at the first-order phase transition are avoided by using dense tables that approximate discontinuous EoSs in a smooth way.

### 3. Uniformly Rotating Stars

We study properties of cold relativistic non-rotating and uniformly rotating stars modeled as stationary, ideal fluid distributions in general relativity using the publicly available RNS code (Cook et al. 1994; Stergioulas & Friedman 1995).

To estimate  $M_{\text{max}}$  we construct sequences of uniformly rotating stars with different central number density  $n_c$  and fixed angular momentum  $J$ . These sequences are bounded from below by the so-called Keplerian or mass-shedding limit in which centrifugal and gravitational forces at the equator of the star exactly cancel. The upper bound of these sequences is determined by BH collapse, which in our setup is either induced by a secular instability or the abrupt softening of the EoS at the phase transition. The onset of the secular instability can be approximately determined with the turning-point

<sup>5</sup> The “soft” (“stiff”) variant is given by the fit 5b (8b) in Jokela et al. (2019). The intermediate EoS was obtained by interpolating between the soft and stiff EoSs, using the fit result 7a from Jokela et al. (2019) as a guiding point.

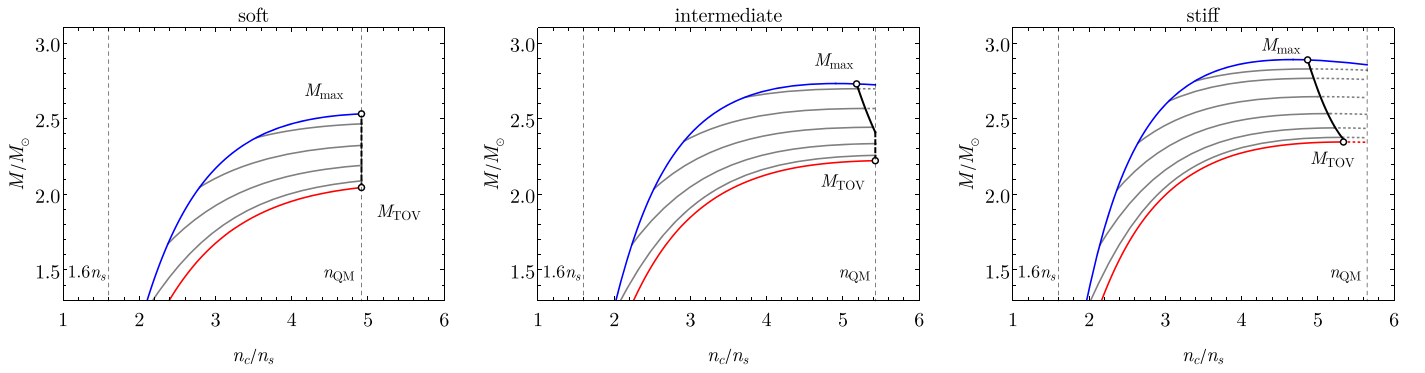


**Figure 2.** Mass as function of the central number density  $n_c$  in units of the saturation density  $n_s$  for soft (left panel), intermediate (middle panel) and stiff (right panel) EoS. Red (blue) curves are for non-rotating (maximally rotating) configurations, vertical dashed lines indicate the matching density  $1.6n_s$  and the density at the deconfinement phase transition  $n_{\text{QM}}$ . Gray lines are sequences with constant angular momentum. Black solid (dashed) curves mark the onset of the secular (phase transition induced) instability.

criterion (Friedman et al. 1988)

$$\left. \frac{\partial M(n_c, J)}{\partial n_c} \right|_{J=\text{const.}} = 0. \quad (1)$$

For non-rotating ( $J=0$ ) stars (1) is necessary and sufficient to determine  $M_{\text{TOV}}$ . For rotating stars the turning-point criterion is only sufficient, but not necessary, i.e., rotating stars that are stable according to (1) can still be dynamically unstable and the onset of instability can appear at densities slightly lower than the turning-point density (Takami et al. 2011). In this work we neglect dynamical instabilities and approximate  $M_{\text{max}}$  by intersecting the Keplerian sequence either with lines constructed from (1) or with the number density at the phase transition  $n_{\text{QM}}$ . In the next section we show examples where both possibilities are realized, including a “mixed” case where  $M_{\text{TOV}}$  is determined by the phase transition and  $M_{\text{max}}$  by the secular instability.

#### 4. Results

In Figure 2 we show the masses of uniformly rotating NSs as a function of the central baryon number density for the three variants of EoS. For the soft EoS (left panel) the onset of instability (black dashed line) is due to the abrupt softening of the EoS as the nuclear to quark matter transition is reached, independently of the angular momentum of the star. In contrast to Paschalidis et al. (2018), Montana et al. (2019), and Bozzola et al. (2019), the holographic model predicts no stable twin or hybrid star solutions.

For the stiff EoS (right panel), however, the secular instability (black solid curve) is reached at densities below the transition density  $n_{\text{QM}}$ . The intermediate EoS shows the “mixed” behavior where the onset of instability is due to the phase transition (secular instability) for slowly (rapidly) rotating stars.

Supramassive neutron stars (SMNS), i.e., axisymmetrically rotating NSs with mass  $M_{\text{TOV}} \leq M \leq M_{\text{max}}$ , are expected to form in low- and intermediate-mass NS binary systems  $M/M_{\text{TOV}} \lesssim 1.5$  (Baiotti & Rezzolla 2017). During its dynamic evolution a SMNS can lose angular momentum by a number of mechanisms (electromagnetic emission, neutrino losses, etc.) until it either ends up as stable, non-rotating NS or reaches a point of instability where it collapses into a BH. In the latter case the lifetime of the star depends strongly on the high-

density part of the EoS where non-perturbative effects such as the deconfinement phase transition are crucial. Our stars collapse because they reach the phase transition or the turning-point line. This picture arises from studies of the merger with numerical general relativity, which for simplicity neglect the physical influence of bulk viscosity, neutrinos, and magnetic fields.

By monotonicity of the turning-point line, it is sufficient to check if  $M_{\text{TOV}}$  is located at a turning point to exclude the possibility of a phase transition induced collapse for all rotating NS, as is the case, for example, in the stiff model shown in Figure 2 (right panel).

The quadrants in Figure 3 show the number density profile of a static star (left) and a star, spinning around the  $z$ -axis at Keplerian, mass-shedding frequency  $f_{\text{max}}$  (right) for two choices for the mass.

Notice that almost all matter in the cores of the stars is described by the holographic model; the dashed black line indicates the  $n = 1.6n_s$  iso-number density surface at which APR transitions to the V-QCD EoS. In the non-rotating configuration with  $M = 1.4 M_{\odot}$  ( $M = 2 M_{\odot}$ )  $R_{\text{match}}/R_e = 0.85$  ( $R_{\text{match}}/R_e = 0.90$ ), where  $R_e$  and  $R_{\text{match}}$  are the maximal radius and the radius at matching density in the equatorial plane, respectively. In Figure 4 we show mass–radius relations for the three holographic EoSs and compare them to the results from GW190814 and a selection of other measurements of NS masses and radii. The static stars in the soft model (solid red curve in the right plot) reach the maximum mass  $M_{\text{TOV}} = 2.04 M_{\odot}$ , a value only barely consistent with direct mass measurements<sup>6</sup> and the bound derived in (Most et al. 2020) based on the GW190814 event, shown as light-blue and light-red bands, respectively. We also notice that all stable stars consistent with the GW190814 measurement (i.e., within the light-green band) are almost maximally rotating. The other models (intermediate and stiff) satisfy these bounds easily, but even for the stiff model high-rotation frequencies  $\gtrsim 1$  kHz are required to reach the green band. This is well above the frequency  $f = 716$  Hz of the fastest spinning pulsar observed so far, PSR J1748-2446ad (Hessels et al. 2006).

There are also estimates for the radii of NSs using the X-ray channel. We show the results from the measurement of PSR J0030+0451 ( $f = 205$  Hz) by the the Neutron star Interior

<sup>6</sup> We show only the result from Cromartie et al. (2019). At  $1\sigma$  level the other measurements mentioned in the introduction do not affect the constraint on the maximum mass significantly.

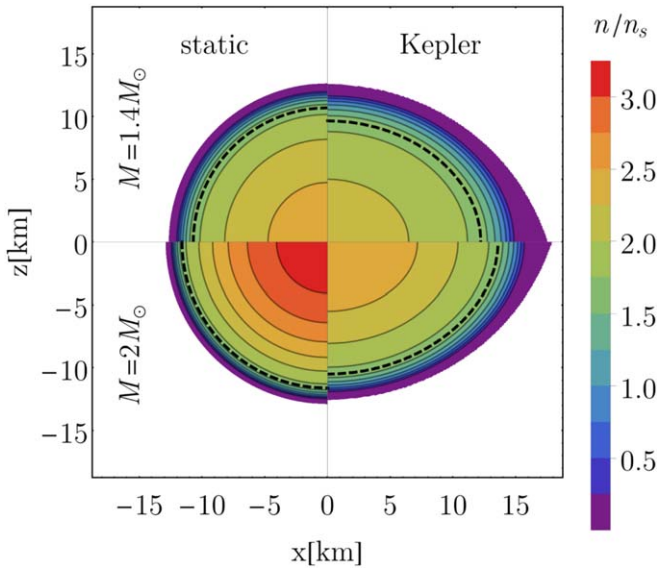


**Figure 3.** Density profile of static (left) and maximally rotating (right) stars with  $1.4 M_{\odot}$  (top) and  $2 M_{\odot}$  (bottom) for the stiff model. The black dashed line is the isocontour at matching density  $n = 1.6 n_s$  and in white regions  $n/n_s < 10^{-13}$ .

Composition Explorer (NICER) Collaboration (Miller et al. 2019; Riley et al. 2019) as well as the measurements of the low-mass X-ray binary 4U 1702-429 ( $f = 329$  Hz) obtained by the Rossi X-Ray Timing Explorer (Nättilä et al. 2017). Our results for slowly rotating NSs agree well with the NICER analysis. Sequences with  $f = 329$  Hz (cyan) constructed from the soft and intermediate model are consistent with the constraint by Nättilä et al. (2017). Although we find stiff models to be disfavored, we do not regard them as excluded at this point, because the constraint is based on a number of model assumptions and because the tension may be alleviated by changes in the crust EoS; see Jokela et al. (2020) and the discussion in the Appendix.

In addition to the three holographic EoSs of Figure 1, we have carried out a scan over all EoSs constructed in Jokela et al. (2020), which span the light red band in Figure 1. Apart from APR, these additional EoSs use the following nuclear matter models at low density: the soft and intermediate variants of the Hebeler–Lattimer–Pethick–Schwenk (Hebeler et al. 2013), Skyrme Lyon (Douchin & Haensel 2001), and IUf (Fattoyev et al. 2010; Hempel & Schaffner-Bielich 2010). We also allowed the matching density  $n_{\text{tr}}$  to vary within the range from  $1.3 n_s$  to  $2.2 n_s$  and required that the EoSs comply with the LIGO/Virgo bound  $\Lambda_{1.4} < 580$  (Abbott et al. 2018). Our results for the distribution of the mass ratio  $M_{\text{max}}/M_{\text{TOV}}$  and the maximum non-rotating mass  $M_{\text{TOV}}$  are shown in Figure 5. The mass ratios are mildly shifted upward with respect to the fit  $M_{\text{max}}/M_{\text{TOV}} = 1.203 \pm 0.022$  for EoSs without a deconfinement transition (green dashed line and band; Breu & Rezzolla 2016). We stress that this happens even though our NSs are fully hadronic; for models admitting hybrid stars with quark matter cores, larger deviations are possible (Bozzola et al. 2019). Consequently, some of the EoSs with the soft variant of V-QCD lie slightly below the estimate of the lowest possible  $M_{\text{TOV}}$  (blue dashed line and band) from Most et al. (2020). Moreover, we note that the stiffest holographic EoSs are able to produce stable NSs a bit above the bound  $M_{\text{TOV}} < 2.16_{-0.15}^{+0.17} M_{\odot}$  of Rezzolla et al. (2018; red dashed line

and band) and the estimate  $M_{\text{TOV}} \lesssim 2.3 M_{\odot}$  of Shibata et al. (2019). At the current stage we do not regard the heavier stars as excluded, because the aforementioned upper bounds dependent on a number of assumptions and uncertainties for example in the modeling of the kilonova or the numerical treatment that neglects viscous effects (Alford et al. 2018), which could significantly affect the bounds.

In order to compare directly to the result of Breu & Rezzolla (2016), we fitted the dependence of  $M_{\text{crit}}$  on the scaled angular momentum  $j = J/M_{\text{crit}}^2$ , where  $M_{\text{crit}}$  is the value of the mass at the onset of instability, given as the black curves in Figure 2. We used the data for all EoSs shown with filled colored markers in Figure 5. The fit to the formula (Breu & Rezzolla 2016)

$$\frac{M_{\text{crit}}}{M_{\text{TOV}}} = 1 + a_2 \left( \frac{j}{j_{\text{Kep}}} \right)^2 + a_4 \left( \frac{j}{j_{\text{Kep}}} \right)^4, \quad (2)$$

where  $j_{\text{Kep}}$  is the value at the intersection with the Keplerian curve, gives  $a_2 = 0.1603$  and  $a_4 = 0.0667$ . Evaluating this fit at  $j = j_{\text{Kep}}$  we obtain the estimate

$$\frac{M_{\text{max}}}{M_{\text{TOV}}} = 1.227_{-0.016}^{+0.031}, \quad (3)$$

where the error bars indicate the largest deviation from the fit.

In addition, we estimate the average ratio of the maximum rest mass  $M_{\text{b,max}}$  and  $M_{\text{max}}$  for all our EoSs

$$\frac{M_{\text{b,max}}}{M_{\text{max}}} = 1.177_{-0.020}^{+0.018}, \quad (4)$$

where the error bars again indicate the largest deviation from the central value. Also, here our value is slightly above the value  $1.171_{-0.014}^{+0.014}$  (two sigma level) obtained in Rezzolla et al. (2018) for EoSs without phase transition.

A summary of salient features of rotating and non-rotating stars is given in the Appendix.

## 5. Conclusion

In this Letter, we analyzed spinning hadronic NSs with EoSs having a deconfinement transition from nuclear to quark matter. The analysis was made possible by using state-of-the-art holographic models for dense QCD, which include both the nuclear and quark matter phases (V-QCD), and therefore give controlled predictions for the properties of the phase transition. The phase transition is strongly first order as the EoS in the nuclear matter (quark matter) phase is relatively stiff (soft). Interestingly, this picture is similar to what arises in another non-perturbative approach, i.e., the functional renormalization group method (Drews & Weise 2017; Otto et al. 2020).

Apart from the phase transition, the holographic models predict that the nuclear matter EoSs is relatively stiff at high densities, making it easy to reach high masses for both non-rotating and rotating NSs. For stiff variants of the model, we find that the maximal masses of non-rotating (rotating) stars are around 2.35 (2.9) solar masses. Therefore, these models are easily consistent with the interpretation (Dexheimer et al. 2020; Most et al. 2020) that the secondary component of the binary merger event GW190814 is a rapidly spinning NS. However, even for the stiffest EoSs the frequencies required for this interpretation are high: we find that  $f \gtrsim 1$  kHz, which is close to the mass-shedding limit ( $\sim 1.5$  kHz) and clearly above the

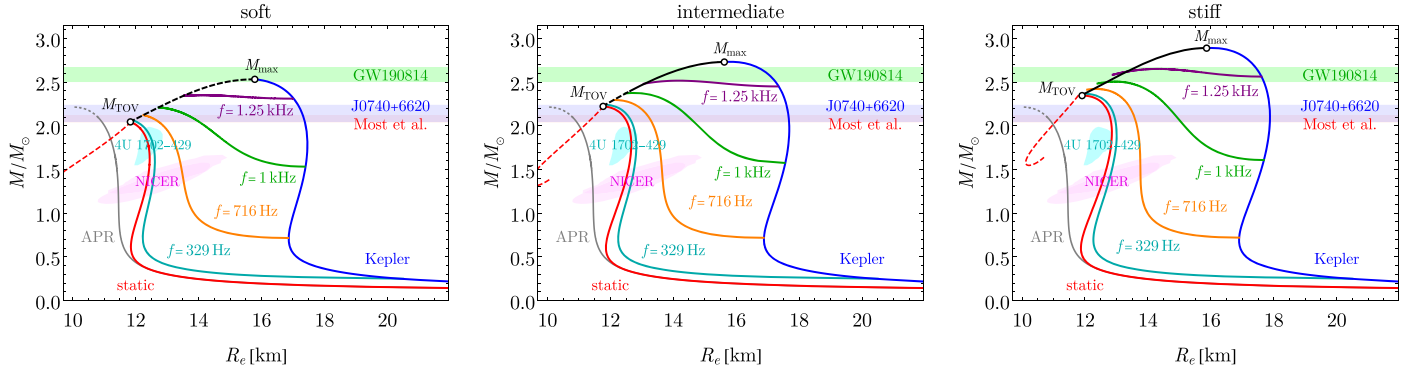


**Figure 4.** Mass–radius relations for soft (left panel), intermediate (middle panel) and stiff (right panel) EoS. Red (blue) curves are for non-rotating (maximally rotating) configurations, the red dashed line is the unstable branch in the quark matter phase, and cyan, orange, green, and purple lines are sequences of fixed rotational frequency. The horizontal bands show the result for the mass of the secondary component of GW190814 (light green) and the most stringent bounds on the maximum mass of static NSs (light blue and light red; Cromartie et al. 2019; Most et al. 2020). In addition, we show observational bounds deduced from PSR J0030+0451 by the Neutron star Interior Composition Explorer (NICER; Miller et al. 2019; Riley et al. 2019; pink ellipses) and from the measurement of the X-ray binary 4U 1702-429 (Nättilä et al. 2017; cyan area).

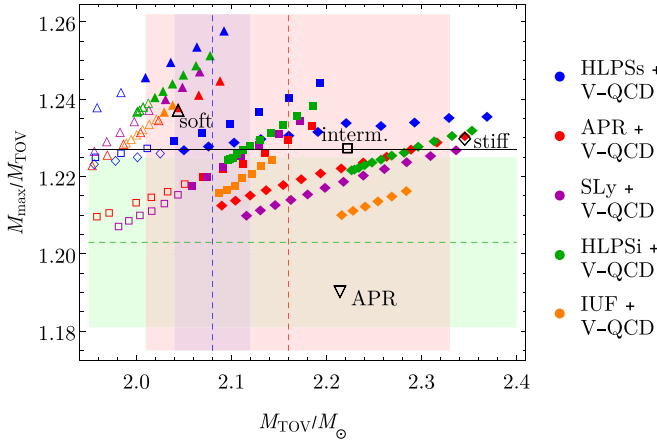


**Figure 5.** Mass ratio  $M_{\max}/M_{\text{TOV}}$  vs.  $M_{\text{TOV}}$  for an ensemble of hybrid EoS from Jokela et al. (2020). The colored markers show the results for different low-density nuclear matter models, indicated in the legend, as the matching density  $n_{\text{tr}}$  varies. Triangles, squares, and diamonds use soft, intermediate, and stiff versions of the holographic model, respectively. The filled (open) markers are EoSs for which the Keplerian curve reaches (fails to reach) the GW190814 band in Figure 4. The EoSs used in the other figures are shown with large black open markers. The green, blue, and red bands show the estimates for the mass ratio (Breu & Rezzolla 2016), minimum of  $M_{\text{TOV}}$  based on GW190814 (Most et al. 2020), and maximum of  $M_{\text{TOV}}$  (Rezzolla et al. 2018), respectively. The horizontal black line shows our fit result from (3).

fastest pulsar rotation frequency observed so far, 716 Hz (Hessels et al. 2006).

Curiously, in the three models considered in this work the maximal masses of rotating and non-rotating stars are determined in different ways. In the soft model, both  $M_{\text{TOV}}$  and  $M_{\max}$ , are determined by the phase transition. In the intermediate model,  $M_{\text{TOV}}$  is determined by the phase transition and  $M_{\max}$  of rapidly rotating stars by the secular instability. In the stiff model, both  $M_{\text{TOV}}$  and  $M_{\max}$  are determined by the secular instability. We find it is sufficient to check if  $M_{\text{TOV}}$  is located at a turning point to exclude the possibility of a phase transition induced collapse for all rotating NSs for a given EoS. Consequently, SMNSs formed in binary NS mergers with EoS satisfying this simple criterion will not produce any signatures of the phase transition in their gravitational wave signal.

Interestingly, we find the ratio of maximal masses of rotating versus non-rotating models to be relatively high compared to models without deconfinement transition (Breu &

Rezzolla 2016); our fit result  $M_{\max}/M_{\text{TOV}} = 1.227^{+0.031}_{-0.016}$  is shifted upward with respect to their result,  $1.203^{+0.022}_{-0.022}$ . This feature is pronounced for EoSs with the soft variant, which can reach  $M_{\max}/M_{\text{TOV}} \approx 1.26$ . Notice that it is indeed the soft variants where both  $M_{\max}$  and  $M_{\text{TOV}}$  are determined by the instability induced by the phase transition, which supports the interpretation that the large values for the ratio arise due to the transition.

In this Letter, we neglected some well-known effects due to computational simplicity. First, we used the turning-point criterion (1) to estimate the onset of the secular instability. To improve on this, we would need to study the impact of dynamical instabilities on our results by carrying out 3 + 1 dimensional simulations. We expect, however, that carrying out the full analysis would change our results very little, because the mass of the NS is insensitive to the exact value of the critical central density near the onset of the instability (see, e.g., Takami et al. 2011). Second, we studied rigidly rotating stars only. It would be interesting to generalize our work to differentially rotating stars for which a similar universal ratio  $M_{\max, \text{dr}}/M_{\text{TOV}} = 1.54^{+0.05}_{-0.05}$  has been proposed Weih et al. (2018). We hope to return to this topic in future work.

We thank Niko Jokela, Antonios Nathanail, Luciano Rezzolla, and Lukas Weih for useful discussions and comments on the manuscript. T.D. was partially supported by the Israel Science Foundation (ISF) grant #1635/16 and the BSF grants #2015626 and #2018722. The work of M.J. was supported in part by a center of excellence supported by the ISF grant #2289/18. This research was also supported by an appointment to the JRG Program at the APCTP through the Science and Technology Promotion Fund and Lottery Fund of the Korean Government. In addition, the research was supported by the Korean Local Governments—Gyeongsangbuk-do Province and Pohang City.

## Appendix Properties of Static and Rotating Stars

In this Appendix we discuss some of the basic features of both non-rotating and rotating NSs. The numbers are listed in Table 1 for the EoSs used in the letter, i.e., the soft, intermediate, and stiff hybrid (APR+V-QCD) EoSs as well as the “pure” APR EoS. The variables used in the table are the

**Table 1**  
Properties of Neutron Stars for the EoSs in This Letter

Model	$\frac{n_{\text{QM}}}{n_s}$	$\frac{M_{\text{TOV}}}{M_{\odot}}$	$\frac{M_{\text{max}}}{M_{\text{TOV}}}$	$\frac{M_{\text{b,max}}}{M_{\text{max}}}$	$\frac{R_{e,1.4}}{\text{km}}$	$\Lambda_{1.4}$	$f_{\text{max}}$ kHz	$c_s^{\text{max}}$
soft	4.89	2.04	1.238	1.172	[12.38, 17.33]	493	1.45	0.65
interm.	5.43	2.22	1.228	1.186	[12.51, 17.44]	536	1.54	0.72
stiff	5.61	2.35	1.231	1.194	[12.60, 17.52]	567	1.60	0.76
APR	...	2.21	1.192	1.202	[11.40, 16.14]	260	2.01	>1

deconfinement phase transition ( $n_{\text{QM}}$ ), maximum mass of non-spinning ( $M_{\text{TOV}}$ ) and spinning ( $M_{\text{max}}$ ) stars, the maximum rest mass ( $M_{\text{b,max}}$ ) of spinning stars, range of equatorial radii ( $R_e$ ) and tidal deformability ( $\Lambda_{1.4}$ ) of  $1.4 M_{\odot}$  stars, maximum rotation frequency ( $f_{\text{max}}$ ) and maximum speed of sound ( $c_s^{\text{max}}$ ). We remark that even the soft version of the hybrid holographic EoS is clearly stiffer than pure APR: the hybrid EoSs give significantly larger values for the tidal deformability and the equatorial radii of both non-rotating and rotating stars at  $M = 1.4 M_{\odot}$ . Notice also that some of the observables presented in the table (such as the radii and the tidal deformability) slightly depend on the crust EoS. For example, varying the crust EoS and the matching density would allow for non-rotating stars with radii below 12 km (Jokela et al. 2020). The masses of heavier NSs (with masses above  $2M_{\odot}$ ) are much less sensitive to the crust, and the same applies to the mass ratios for which we already analyzed the dependence on the crust in Figure 5.

### ORCID iDs

Tuna Demircik  <https://orcid.org/0000-0003-4791-3846>  
 Christian Ecker  <https://orcid.org/0000-0002-8669-4300>  
 Matti Järvinen  <https://orcid.org/0000-0002-9916-6275>

### References

- Abbott, B., Abbott, R., Abbott, T. D., et al. 2018, *PhRvL*, **121**, 161101  
 Abbott, R., Abbott, T. D., Abraham, S., et al. 2020, *ApJL*, **896**, L44  
 Akmal, A., Pandharipande, V., & Ravenhall, D. 1998, *PhRvC*, **58**, 1804  
 Alford, M. G., Bovard, L., Hanauske, M., Rezzolla, L., & Schwenzer, K. 2018, *PhRvL*, **120**, 041101  
 Alford, M. G., Han, S., & Prakash, M. 2013, *PhRvD*, **88**, 083013  
 Annala, E., Gorda, T., Kurkela, A., & Vuorinen, A. 2018, *PhRvL*, **120**, 172703  
 Antoniadis, J., Freire, P. C. C., Wex, N., et al. 2013, *Sci*, **340**, 6131  
 Arzoumanian, Z., Brazier, A., Burke-Spolaor, S., et al. 2018, *ApJS*, **235**, 37  
 Baiotti, L., & Rezzolla, L. 2017, *RPPH*, **80**, 096901  
 Bauswein, A., Bastian, N.-U. F., Blaschke, D. B., et al. 2019, *PhRvL*, **122**, 061102  
 Bigazzi, F., Casero, R., Cotrone, A. L., Kiritsis, E., & Paredes, A. 2005, *JHEP*, **10**, 012  
 Borsanyi, S., Fodor, Z., Hoelbling, C., et al. 2014, *PhLB*, **730**, 99  
 Borsanyi, S., Fodor, Z., Katz, S. D., et al. 2012, *JHEP*, **01**, 138  
 Bozzola, G., Espino, P. L., Lewin, C. D., & Paschalidis, V. 2019, *EPJA*, **55**, 149  
 Breu, C., & Rezzolla, L. 2016, *MNRAS*, **459**, 646  
 Casero, R., Kiritsis, E., & Paredes, A. 2007, *NuPhB*, **787**, 98  
 Chesler, P. M., Jokela, N., Loeb, A., & Vuorinen, A. 2019, *PhRvD*, **100**, 066027  
 Cook, G. B., Shapiro, S. L., & Teukolsky, S. A. 1994, *ApJ*, **424**, 823  
 Cromartie, H. T., Fonseca, E., Ransom, S. M., et al. 2019, *NatAs*, **4**, 72  
 DeWolfe, O., Gubser, S. S., & Rosen, C. 2011a, *PhRvD*, **83**, 086005  
 DeWolfe, O., Gubser, S. S., & Rosen, C. 2011b, *PhRvD*, **84**, 126014  
 Dexheimer, V., Gomes, R., Klähn, T., Han, S., & Salinas, M. 2020, arXiv:2007.08493  
 Douchin, F., & Haensel, P. 2001, *A&A*, **380**, 151  
 Drews, M., & Weise, W. 2017, *PrPNP*, **93**, 69  
 Ecker, C., Järvinen, M., Nijs, G., & van der Schee, W. 2020, *PhRvD*, **101**, 103006  
 Essick, R., & Landry, P. 2020, *ApJ*, **904**, 80  
 Fattoyev, F., Horowitz, C., Piekarewicz, J., & Reed, B. 2002, *PhRvC*, **102**, 065805  
 Fattoyev, F., Horowitz, C., Piekarewicz, J., & Shen, G. 2010, *PhRvC*, **82**, 055803  
 Friedman, J. L., Ipser, J. R., & Sorkin, R. D. 1988, *ApJ*, **325**, 722  
 Godzieba, D. A., Radice, D., & Bernuzzi, S. 2020, arXiv:2007.10999  
 Gürsoy, U., & Kiritsis, E. 2008, *JHEP*, **02**, 032  
 Hebeler, K., Lattimer, J., Pethick, C., & Schwenk, A. 2013, *ApJ*, **773**, 11  
 Hempel, M., & Schaffner-Bielich, J. 2010, *NuPhA*, **837**, 210  
 Hessels, J. W., Ransom, S. M., Stairs, I. H., et al. 2006, *Sci*, **311**, 1901  
 Hoyos, C., Jokela, N., Järvinen, M., et al. 2020, *PhRvL*, **125**, 241601  
 Ishii, T., Järvinen, M., & Nijs, G. 2019, *JHEP*, **07**, 003  
 Järvinen, M., & Kiritsis, E. 2012, *JHEP*, **03**, 002  
 Jokela, N., Järvinen, M., Nijs, G., & Remes, J. 2020, arXiv:2006.01141  
 Jokela, N., Järvinen, M., & Remes, J. 2019, *JHEP*, **03**, 041  
 Kurkela, A., Fraga, E. S., Schaffner-Bielich, J., & Vuorinen, A. 2014, *ApJ*, **789**, 127  
 Kurkela, A., Romatschke, P., & Vuorinen, A. 2010, *PhRvD*, **81**, 105021  
 Miller, M., Lamb, F. K., Dittmann, A. J., et al. 2019, *ApJL*, **887**, L24  
 Montana, G., Tolos, L., Hanauske, M., & Rezzolla, L. 2019, *PhRvD*, **99**, 103009  
 Most, E. R., Papenfort, L. J., Dexheimer, V., et al. 2019, *PhRvL*, **122**, 061101  
 Most, E. R., Papenfort, L. J., Weih, L. R., & Rezzolla, L. 2020, *MNRAS: Letters*, **499**, L82  
 Nättälä, J., Miller, M., Steiner, A., et al. 2017, *A&A*, **608**, A31  
 O’Boyle, M. F., Markakis, C., Stergioulas, N., & Read, J. S. 2020, *PhRvD*, **102**, 083027  
 Otto, K., Oertel, M., & Schaefer, B.-J. 2020, *PhRvD*, **101**, 103021  
 Panero, M. 2009, *PhRvL*, **103**, 232001  
 Paschalidis, V., Yagi, K., Alvarez-Castillo, D., Blaschke, D. B., & Sedrakian, A. 2018, *PhRvD*, **97**, 084038  
 Rezzolla, L., Most, E. R., & Weih, L. R. 2018, *ApJL*, **852**, L25  
 Riley, T. E., Watts, A. L., Bogdanov, S., et al. 2019, *ApJL*, **887**, L21  
 Roupas, Z. 2021, *Ap&SS*, **366**, 9  
 Safarzadeh, M., & Loeb, A. 2020, *ApJL*, **899**, L15  
 Shibata, M., Zhou, E., Kiuchi, K., & Fujibayashi, S. 2019, *PhRvD*, **100**, 023015  
 Stergioulas, N., & Friedman, J. 1995, *ApJ*, **444**, 306  
 Takami, K., Rezzolla, L., & Yoshida, S. 2011, *MNRAS*, **416**, L1  
 Tan, H., Noronha-Hostler, J., & Yunes, N. 2020, *PhRvL*, **125**, 261104  
 Tews, I., Krüger, T., Hebeler, K., & Schwenk, A. 2013, *PhRvL*, **110**, 032504  
 Tews, I., Pang, P. T., Dietrich, T., et al. 2020, arXiv:2007.06057  
 Vattis, K., Goldstein, I. S., & Koushiappas, S. M. 2020, *PhRvD*, **102**, 061301  
 Weih, L. R., Hanauske, M., & Rezzolla, L. 2020, *PhRvL*, **124**, 171103  
 Weih, L. R., Most, E. R., & Rezzolla, L. 2018, *MNRAS*, **473**, L126  
 Weissenborn, S., Sagert, I., Pagliara, G., Hempel, M., & Schaffner-Bielich, J. 2011, *ApJL*, **740**, L14  
 Zhang, N.-B., & Li, B.-A. 2020, *ApJ*, **902**, 38